

Proximity-Induced Superconductivity in Scalable Topological Insulator/Graphene/Gallium Heterostructures

Cequn Li¹, Yi-Fan Zhao¹, Alexander Vera^{2,3,4}, Omri Lesser⁵, Hemian Yi¹, Shalini Kumari^{2,3,4}, Zijie Yan¹, Chengye Dong^{2,3,4}, Timothy Bowen^{2,3,4}, Ke Wang⁶, Haiying Wang⁶, Kenji Watanabe⁷, Takashi Taniguchi⁸, Yuval Oreg⁵, Joshua A. Robinson^{2,3,6,9,10}, Cui-Zu Chang¹, and Jun Zhu^{1,2*}

1. Department of Physics, The Pennsylvania State University, University Park, PA 16802, USA
2. Center for 2-Dimensional and Layered Materials, The Pennsylvania State University, University Park, PA 16802, USA
3. Department of Materials Science and Engineering, The Pennsylvania State University, University Park, PA 16802, USA
4. Center for Nanoscale Science, The Pennsylvania State University, University Park, PA 16802, USA
5. Department of Condensed Matter Physics, Weizmann Institute of Science, Rehovot 760001, Israel
6. Materials Research Institute, The Pennsylvania State University, University Park, PA 16802, USA
7. Research Center for Functional Materials, National Institute for Materials Science, 1-1 Namiki, Tsukuba 305-0044, Japan
8. International Center for Materials Nanoarchitectonics, National Institute for Materials Science, 1-1 Namiki, Tsukuba 305-0044, Japan.
9. Department of Chemistry, The Pennsylvania State University, University Park, PA 16802, USA
10. 2-Dimensional Crystal Consortium, The Pennsylvania State University, University Park, PA 16802, USA.

* Correspondence to: jzhu@phys.psu.edu (J. Zhu)

The introduction of superconductivity to the Dirac surface states of a topological insulator leads to a novel state of matter known as a topological superconductor^{1, 2}. A topological superconductor may host Majorana zero modes, the braiding of which is a cornerstone operation of a topological qubit^{3, 4}. The development of a scalable material platform is key to the realization of topological quantum computing⁵⁻⁷. Here we report on the growth and properties of high-quality (Bi,Sb)₂Te₃/graphene/gallium heterostructures. Our novel synthetic approach enables atomically sharp layers at both hetero-interfaces, which in turn

promotes proximity-induced superconductivity that originates in the gallium film. A lithography-free, van der Waals tunnel junction is developed to perform transport tunneling spectroscopy. Our results show a robust, proximity-induced superconducting gap formed in the Dirac surface states in 5-10 quintuple-layer (Bi,Sb)₂Te₃/graphene/gallium heterostructures. The motion of a single Abrikosov vortex, where the Majorana zero modes are expected to reside, manifests in discrete conductance changes. The epitaxial thin-film (Bi,Sb)₂Te₃/graphene/gallium platform opens up new avenues for understanding topological superconductivity and realizing Majorana braiding circuitry.

A primary approach to realize topological superconductivity (TSC) in a potentially scalable material platform is to exploit the superconducting proximity effect of a hybrid system involving an s-wave superconductor (SC), and a 1D/2D semiconductor with strong spin-orbit coupling^{5, 8-10}. Studies following this approach have made much progress in fundamental science and materials engineering, but have also encountered great challenges⁷. As envisioned by Fu and Kane¹, TSC is also predicted to occur in a topological insulator (TI)-SC hybrid system, where the lifting of the spin degeneracy, a key ingredient for TSC, is already achieved in the helical surface states of a topological insulator. Scanning tunneling microscopy studies have reported proximity-induced SC and signatures of Majorana zero modes (MZM) in TI/SC heterostructures¹¹⁻¹⁵. However, the difficulty of creating high-quality, scalable platforms remains a major roadblock to further experimentation. A high-quality TI film can be grown on bulk NbSe₂^{11, 12, 16}, but does not form a clean hetero-junction on metallic film superconductors such as Al or Nb due to interfacial reactions¹⁷⁻²¹. In addition, to prevent the oxidization of TI films is a challenge in device fabrication.

Transport studies, a major experimental probe of MZM, remain limited in TI/SC heterostructures^{18, 20-22}.

In this work, we demonstrate the synthesis of epitaxial (Bi,Sb)₂Te₃/graphene/Gallium (BST/Gr/Ga) thin films with atomically sharp hetero-interfaces. We construct clean van der Waals (vdW) tunnel junctions and employ transport tunneling spectroscopy to probe their superconducting properties. Tunneling spectra obtained on heterostructures with the BST thickness ranging from 5 to 10 quintuple layers (QLs) exhibit the characteristics of two superconducting gaps. The larger gap originates from the superconducting Ga film²³. We attribute the smaller gap, which is 30-50% of the gap in Ga, to proximity-induced superconductivity in the Dirac surface states of the BST film. The introduction of magnetic vortex leads to discrete tunneling conductance jumps, with the smallest unit corresponding to the motion of a single flux quantum. Our experiments established a new scalable TI/SC platform for the studies of TSC and Majorana physics.

As illustrated in Fig. 1a, BST/Gr/Ga heterostructures are synthesized in two steps. We first grow a two-atomic-layer-thin (2L) Ga film capped by epi-graphene using confinement heteroepitaxy (CHet) recently developed by some of the authors²³. We then grow (Bi,Sb)₂Te₃ of controlled thickness and composition using molecular beam epitaxy (MBE)²⁴. Crucially, the epi-graphene layer acts as a chemical barrier to prevent the formation of Ga-(Bi,Sb) alloys and Ga-Te compound and templates the growth of BST due to their similar lattice structures^{25, 26}. This approach results in abrupt, atomically sharp growth at every hetero-interface, as verified by cross-sectional scanning transmission electron microscopy (STEM) (Fig. 1b). The clean, vdW-like interface

facilitates high-efficiency superconducting proximity coupling²⁷. The grown film is transferred from the MBE chamber to an Ar-filled glovebox without breaking vacuum. We construct a clean vdW tunnel junction consisting of graphite electrode and 1-2 h-BN tunnel barrier²⁹ (Fig. 1d) and transfer the tunnel junction to the BST/Gr/Ga film inside the glovebox (Fig. 1c). The active area is encapsulated by a large h-BN sheet to prevent oxidization before the film is removed from the glovebox and processed into a full device using lithography (Fig. 1e). Fabrication details are given in Section S2 of the Supplementary Information (SI). The use of a vdW tunnel junction preserves the pristine BST surface and enables measurements under a wide range of experimental conditions outside the growth chamber.

In-situ angle-resolved photoemission spectroscopy (ARPES) measurements are performed on grown BST films to examine the film quality and Fermi level placement E_F . Figure 2a shows an exemplary band map of a 5 QL $(\text{Bi}_{0.7}\text{Sb}_{0.3})_2\text{Te}_3/\text{Gr}/\text{Ga}$ film (See Fig. S1 for band maps on 8 and 10QL films). The Dirac surface states (DSS) are sharp and are the only states crossing the Fermi level, which fulfils the prerequisite for the formation of TSC. The Dirac point is located at -205 meV below E_F , which is roughly where the valence band maximum is. The position of E_F is corroborated by differential tunneling conductance dI/dV measurements obtained on the same film and shown in Fig. 2b, using criteria described in the literature^{30, 31}.

Owing to the epi-graphene reaction barrier, the growth of BST preserves the superconductivity of the 2L Ga film²³ extremely well. Temperature- and magnetic field-dependent transport measurements performed on a series of heterostructures with varying BST film thickness consistently show a T_c of 3–4.2 K and an upper critical perpendicular field H_{c2} of 50–80 mT.

Figure 2c plots an example of $R_{xx}(T)$ measured on device 04H-5QL at selected fields. Additional data are given in Section S3 of the SI. Figure 2d plots H_{c2} versus T extracted from Fig. S3c. The linear relationship between H_{c2} and T confirms the 2D nature of the superconductivity³². Our 5QL BST film can support a critical current density J_c as large as $0.14 \text{ A}/\mu\text{m}^2$ (Fig. S3d), which is compared to other elemental superconductor films such as Al and Nb³³.

Next, we perform tunneling spectroscopy measurements on 5QL and 10 QL BST/Gr/Ga films using devices similar to that shown in Fig. 1e. The tunneling process is schematically illustrated in Fig. 3a. The tunneling current can either flow horizontally through the surface states of the BST film or vertically through the bulk to the Ga layer underneath; this allows us to probe the superconductivity of both layers. We have verified the efficacy of the vdW junction by first applying it to a Gr/Ga film and the resulting $dI/dV(V_{dc})$ spectra are shown in Fig. 3b. Both the V-shaped dip near zero bias and the accompanying peaks at finite biases are characteristics of a superconducting gap, as observed in scanning tunneling spectroscopy^{11, 12, 15} or point contact spectroscopy²². Indeed, the tunneling spectra in Fig. 3b can be well fit by a Blonder-Tinkham-Klapwijk (BTK) model³⁴, from which we obtain the temperature-dependent gap $\Delta(T)$, the tunnel barrier transparency Z and the lifetime broadening Γ of the Cooper pairs. (See Section S4 of the SI for details of the BTK model and fits to data.) $\Delta(T)$ is well described by $\Delta(T) = \Delta_0 \tanh(1.74 \sqrt{\frac{T_c}{T}} - 1)$ (Eq. 1), where $T_c = 3.1 \text{ K}$ is from transport studies of the same film and we obtain $\Delta_0 = 0.395 \text{ meV}$ from the fits (Fig. S4). The parameters of the Gr/Ga film serve as important references to the subsequent studies of BST/Gr/Ga films.

Figure 3c plots the T -dependent $dI/dV(V_{dc})$ obtained on device 02T-5QL, which is made on a 5QL BST/Gr/Ga film. We observe the familiar V-shaped dip near zero dc bias and not one, but two high conductance humps at high biases. Both the dip and the humps weaken with increasing temperature and disappear completely above 4 K, which corresponds to the T_c of this film obtained in transport studies (Fig. S3a). Following literature^{35, 36} we model the spectra as a weighted sum of two SC tunneling processes. Exemplary fits to data using a two-gap BTK model are shown in Fig. 3d, from which we obtain and label the two gaps as $\Delta_S = 0.19$ meV and $\Delta_I = 0.5$ meV respectively. Similar fits are obtained at other temperatures and the resulting $\Delta_S(T)$ and $\Delta_I(T)$ are plotted in Fig. 3e. Both $\Delta_S(T)$ and $\Delta_I(T)$ are well described by Eq. (1) with a common T_c of 4.0 K. These analyses strongly suggest that Δ_I originates from the SC gap of the Ga film while Δ_S is induced by the proximity effect.

The structure of our tunnel junction as illustrated in Fig. 3a lends itself to a natural two-gap interpretation, where Δ_I corresponds to the SC gap of the bottom TI/Gr/Ga interface and Δ_S corresponds to the induced gap at the top surface of the BST film, where the Dirac surface states reside. Single electron tunneling into the BST film onsets at $e|V_{dc}| \geq \Delta_S$, where the top surface turns normal; this gives rise to the zero-bias conductance dip and the first set of coherence peaks. At $e|V_{dc}| \geq \Delta_I$, a second tunneling path opens, where an electron can reach the drain electrode through the bulk of the BST film then the normal Ga film. This leads to the second set of coherence peaks. The fits in Fig. 3d illustrate the individual and the sum of the two tunneling processes. The zero-bias conductance dip and the first coherence peaks are almost entirely given by Δ_S , making its value a very robust finding of the analysis. A proximity-induced SC gap is observed on four tunnel junctions made on film 02T-5QL (Fig. 3f) and our analysis gives Δ_S/Δ_I in the range of (37–

$46) \pm 4\%$ (Table S2 of the SI), which is consistent with previous studies performed on $\text{Bi}_2\text{Se}_3/\text{NbSe}_2$ ^{11, 22}, $\text{Bi}_2\text{Te}_3/\text{NbSe}_2$ ¹² and $\text{Bi}_2\text{Se}_3/\text{Nb}$ ¹⁹.

Similar measurements and analysis are performed on two tunnel junctions constructed on 03T-10QL BST/Gr/Ga films, producing Δ_S/Δ_I in the range of $(34-42) \pm 4\%$. These measurements attest to the robustness of the proximity-induced superconductivity in the Dirac surface states of the TI film. A more complete and detailed analysis of the tunneling spectra on 5 and 10QL devices are given in Section S5 of the SI. In our setup, tunneling occurs over an area of approximately $3 \mu\text{m}^2$, where the thickness of the BST film could deviate from its nominal value by 1-2 QL. A more precise study of the dependence of Δ_S on film thickness^{11, 12, 19, 22} will require a different design.

In the remainder of the paper, we show tunneling conductance change due to the motion of Abrikosov vortices, which localize MZMs in a topological superconductor^{1, 13}. A vortex is normal at its core and its presence in the tunneling area A raises the zero-bias tunneling conductance by a certain amount G_{sv} (Fig. 4a). If vortices enter the tunneling junction one by one, we expect the zero-bias dI/dV to increase from its zero-field value in a staircase pattern with an average slope of $\Delta G/\Delta B = \frac{A \times G_{\text{sv}}}{\Phi_0}$, (Eq. 2), where $\Phi_0 = h/2e$ is the magnetic flux quantum. Figure 4b plots the measured zero-bias conductance $dI/dV(B)$ on device 03T-10QL. While the general trend of the data agrees with Eq. (2), the change of conductance with B is not always monotonic and the two field sweep directions show considerable hysteresis, suggesting the trapping of vortices. Further, we observe conductance jumps in multiple integers of G_{sv} , suggesting that multiple vortices move together as a bundle³⁷. The insets of Fig. 4b show examples of $\Delta G = 1, 2, 4, 7 G_{\text{sv}}$. The above characteristics are general to both Gr/Ga and BST/Gr/Ga junctions, where additional data are given

in Section S6 of the SI. These measurements show that transport spectroscopy provides a valuable probe of the vortex dynamics that can be performed concomitantly with current-phase studies in Josephson junctions to examine topological phase transitions and MZMs. These directions will be explored in future studies.

In summary, we demonstrate the growth and characterization of $(\text{Bi,Sb})_2\text{Te}_3/\text{Gr}/\text{Ga}$ thin-film heterostructures, a novel scalable platform that could be exploited to realize topological superconductivity. Using a clean vdW tunnel junction and transport tunneling spectroscopy, we show experimental evidence of a robust proximity-induced superconducting gap in the Dirac surface states of the MBE-grown $(\text{Bi,Sb})_2\text{Te}_3$ film and visualize the motion of Abrikosov vortices down to a single vortex. Our synthetic approach of combining confinement heteroepitaxy and MBE opens the door to the studies of novel superconducting and magnetic heterostructures.

Figures

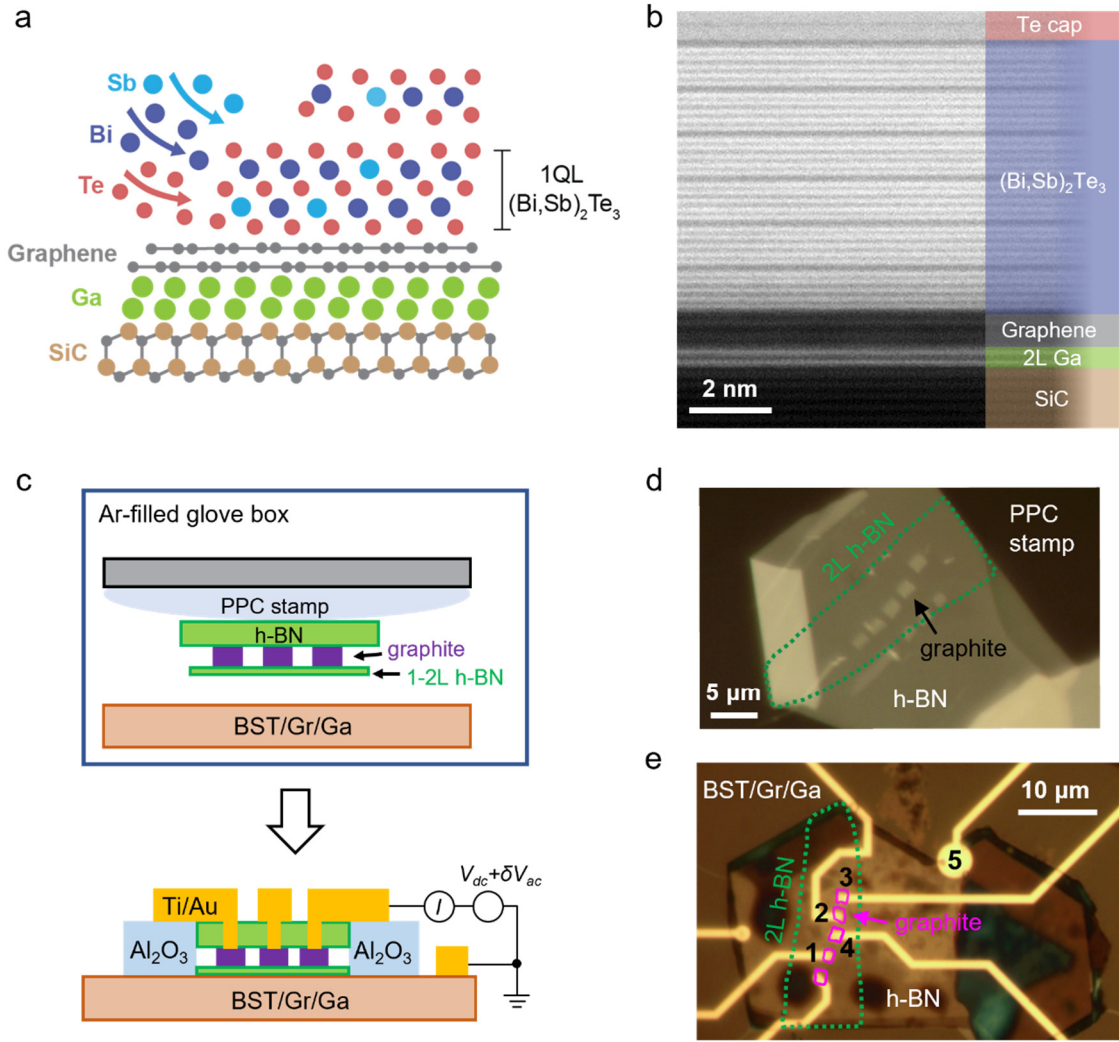


Fig. 1 | Epitaxial growth of BST/Gr/Ga heterostructures and fabrication of tunnel junction devices. **a**, Schematic of the growth combining CHet-growth of Gr/2L-Ga and MBE growth of (Bi,Sb)₂Te₃. **b**, A cross-sectional STEM image showing the atomically sharp hetero-interfaces between 6QL (Bi,Sb)₂Te₃, epi-graphene, and the 2L-Ga. **c**, Schematics of the van der Waals tunnel junction construction, device structure and the differential tunneling conductance measurement setup. **d**, Optical image of an h-BN/graphite/2L h-BN stack on a PPC stamp. The graphite squares are produced by atomic force microscope (AFM) oxidation nanolithography²⁸ and are $\sim 3 \mu\text{m}^2$ in area. **e**, Optical image of device 02T-5QL with four tunnel junctions as labeled. Contacts 1-4 are made to the graphite electrodes and contact 5 directly contacts the BST/Gr/Ga film.

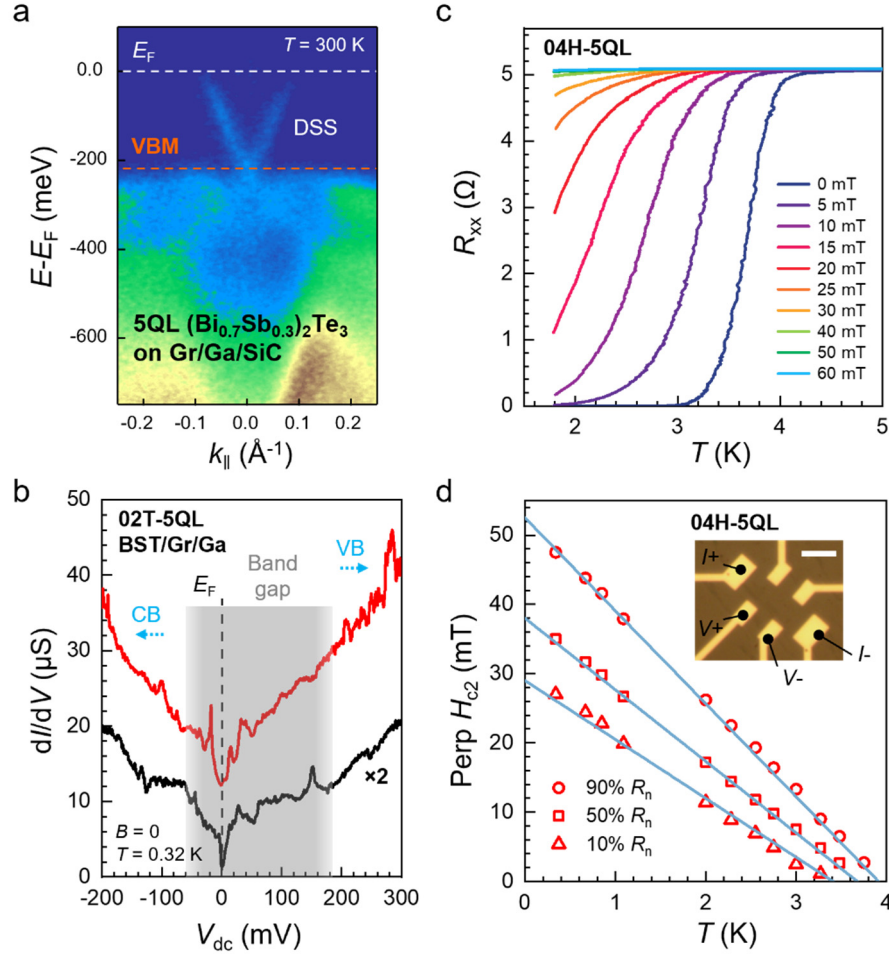


Fig. 2 | Coexistence of Dirac surface states and superconductivity in BST/Gr/Ga heterostructures. **a**, Room-temperature ARPES band map of a 5QL $(\text{Bi}_{0.7}\text{Sb}_{0.3})_2\text{Te}_3/\text{Gr}/\text{Ga}$ film. **b**, dI/dV versus V_{dc} obtained on 02T-5QL made on the same film. Red and black curves are from different junctions. The red curve is shifted vertically by $10 \mu\text{S}$ for clarity. A positive dc bias probes states below the Fermi level. The grey shade box corresponds to the bulk band gap region of the BST film, consistent with the ARPES measurement in **a**. CB and VB represent the locations of the conduction band and the valence band, respectively. **c**, T -dependent R_{xx} obtained on 04H-5QL at selected magnetic fields. The field is applied perpendicular to the film. **d**, Upper critical field H_{c2} as a function of temperature. Solid lines are linear fits using the 2D Ginzburg-Landau model. Values of H_{c2} are read from the measurements shown in Fig. S3c of the SI at fields where R_{xx} reaches 90%, 50% and 10% of the normal state resistance R_n , respectively. The inset shows the optical image of 04H-5QL, where Ti/Au electrodes are directly deposited onto the film. The scale bar is $5 \mu\text{m}$.

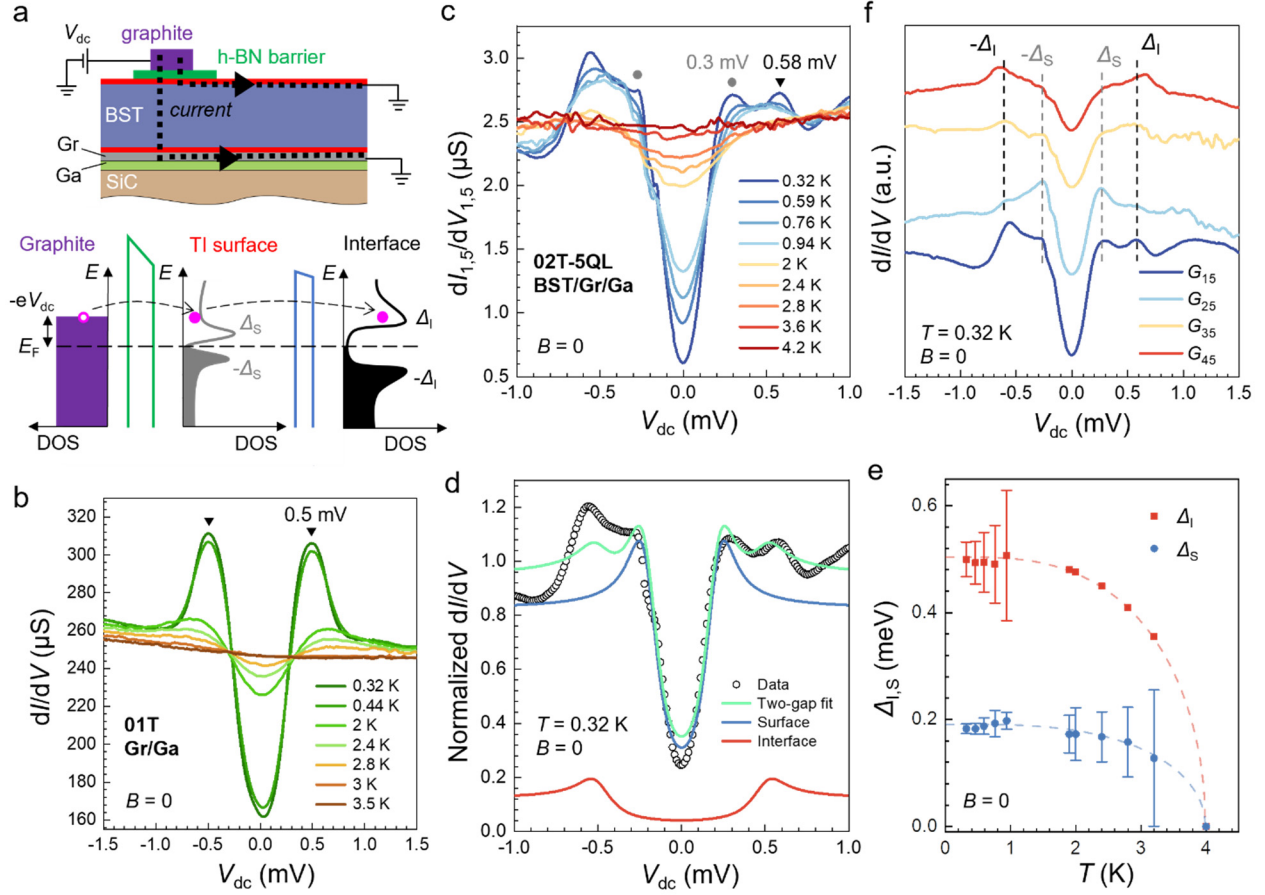


Fig. 3 | Proximity-induced superconductivity in BST/Gr/Ga heterostructures. **a**, Schematic of the two-gap tunneling process and the corresponding density of states diagrams. **b**, $dI/dV(V_{dc})$ obtained on device 01T (Gr/Ga without the growth of BST) at selected temperatures. **c**, $dI/dV(V_{dc})$ obtained on 02T-5QL between contacts 1 and 5 at selected temperatures. We examine the magnetic field dependence of the spectra in Fig. S5b to exclude coincidental features from the fitting, such as the sharp peak at $V_{dc} = -0.6$ mV. **d**, Fits to the 0.32 K data in **c** using a two-gap BTK model showing the contributions from the BST surface tunneling (blue trace), and the BST/Gr/Ga interface tunneling (red trace), and the total (green trace). The spectra weight of the blue trace is 88%. Only data at positive dc biases are fitted. **e**, Δ_S and Δ_I versus temperature obtained from the fitting. The dashed lines plot the BSC temperature dependence of a SC gap given in Eq. (1) with a common T_c of 4 K. At $T \gtrsim 1.9$ K, we fix Δ_I following the red dashed line to obtain more accurate fitting of Δ_S . Error bars represent 95% confidence interval. **f**, $dI/dV(V_{dc})$ obtained on four different junctions on 02T-5QL. Curves are normalized by their normal state conductance and stacked vertically for clarity. All show features associated with two SC gaps. See Figs. S4-6 of the SI for the full BTK analysis on Gr/Ga, 5QL and 10QL BST/Gr/Ga films.

(Single column graph)

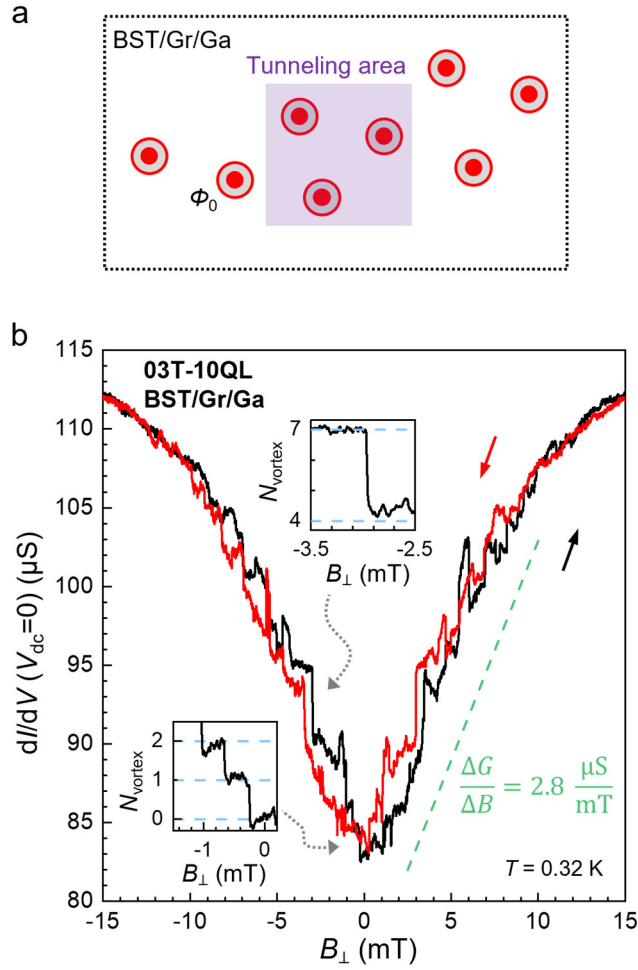


Fig. 4 | Vortex trapping and single vortex motion. **a**, Schematic of Abrikosov vortices penetrating the proximitized BST/Gr/Ga film and enter the tunnel junction area defined by the size of the graphite contact $A \sim 3 \mu\text{m}^2$. **B**, Zero-bias dI/dV measured on field upswing (black trace) and downswing with a rate of $10 \mu\text{T/s}$. From J2 of 03T-10QL. The green dashed line is calculated from Eq. (2) using $A = 3.4 \mu\text{m}^2$ and agrees with data very well. We attribute the smallest conductance step G_{sv} to the effect of a single vortex $G_{sv} = 1.7 \mu\text{S}$ in this device. The vortex number N_{vortex} in the tunneling area is calculated from $N_{\text{vortex}} = (G(B) - G(0 \text{ T}))/G_{sv}$ and labeled in the two insets for conductance plateaus. Conductance change corresponding to a single vortex motion is observed.

Methods

Confinement heteroepitaxy growth of 2D-Ga

Gr/2D-Ga was grown using the CHet process described in Ref. ²³. Briefly, silicon carbide (II-VI Inc.) was diced into 1×0.5 cm or 1×1 cm substrates and pre-cleaned via a 20-minute soak in Nano-Strip (VWR, 90% sulfuric acid, 5% peroxymonosulfuric acid, <1% hydrogen peroxide). Subsequently, mono- or bi-layer epitaxial graphene was synthesized via silicon sublimation from the silicon carbide substrate for 20 minutes at 1800 °C in a 700 Torr argon atmosphere. Prior to intercalation, the graphene was subjected to an oxygen plasma (50 sccm He, 150 sccm O₂ at 500 mTorr and 50 W) in a M4L RF Gas Plasma system for 1 minute to generate defects that serve to facilitate metal diffusion to the graphene/SiC interface.

Intercalation was accomplished in a horizontal quartz tube (22 mm \times 25 mm, inner \times outer diameter) vacuum furnace, where gallium powder (Sigma Aldrich, 99.999% trace metals basis, 30-100 mg) was placed in an alumina crucible directly below a downward facing, plasma-treated EG/SiC substrate. Prior to heating, the tube furnace was evacuated and backfilled with UHP Ar. Finally, the sample and Ga powder were heated to 800 °C for 30 minutes under an UHP Ar or forming gas (3% H₂) environment at 300 – 700 Torr, with 50 sccm total gas flow. The sample was then cooled to room temperature.

MBE growth of (Bi,Sb)₂Te₃

(Bi,Sb)₂Te₃ films were grown in a commercial MBE system (Omicron Lab 10) with a base vacuum better than 2×10^{-10} mbar. Graphene/Ga/SiC substrates were outgassed at ~350 °C for an hour prior to the growth of (Bi,Sb)₂Te₃. High purity Bi(99.9999%), Sb(99.9999%), and Te(99.9999%) were evaporated from Knudsen effusion cells. The flux ratio Te per (Bi + Sb) was set to be greater than 10 to prevent Tellurium deficiency in the film. The substrate was maintained at ~230 °C during growth. The growth rate of the (Bi,Sb)₂Te₃ film was about 0.2 QL/min. Reflection high energy electron diffraction (RHEED) was used to monitor the growth. Grown films were annealed at ~230 °C for 30 minutes to improve the crystal quality before cooling down to room temperature. After *in-situ* ARPES measurements, grown films were transferred to an Argon-filled glovebox using a vacuum suitcase with a base pressure $\sim 5 \times 10^{-8}$ mbar to preserve the pristine (Bi,Sb)₂Te₃ surface.

In-situ APRES

ARPES measurements were performed in a chamber with a base vacuum of $\sim 5 \times 10^{-11}$ mbar. The MBE-grown (Bi,Sb)₂Te₃ films were transferred to the ARPES chamber without breaking the ultrahigh vacuum. The photoelectrons were excited by an unpolarized He-I α light (~21.2 eV), and a Scientia R3000 analyzer was used for the ARPES measurements. The energy and angle resolutions are ~10 meV and ~0.2°, respectively. All ARPES measurements were performed at room temperature.

Cross-sectional STEM

Cross-sectional transmission electron microscopy (TEM) samples were prepared using a FEI Helios 660 focused ion beam (FIB) system. A thick protective amorphous carbon layer was deposited over the region of interest then Ga⁺ ions (30 kV then stepped down to 1 kV to avoid ion

beam damage to the sample surface) were used in the FIB to make the samples electron transparent for TEM images. High resolution scanning transmission electron microscopy (STEM) was performed at 300 kV on a dual spherical aberration-corrected FEI Titan G2 60-300 S/TEM. All the STEM images were collected by using a high angle annular dark field (HAADF) detector with a collection angle of 50-100 mrad.

Transport studies

All measurements were performed in a He-3 cryostat with a base temperature of 320 mK. We measure four-probe resistances using standard low-frequency lock-in techniques with an excitation current of 100 nA. To perform differential conductance measurement, we apply a dc voltage with a small ac modulation of 10-50 μ V to the graphite contacts and measure the ac current using a lock-in amplifier (Stanford Research SR860). To control the magnet field finely, we use a Keithley 2400 sourcemeter to output current to the superconducting solenoid.

Acknowledgements

C.L., H.Y., C.-Z.C. S.K., T.B., J.A.R., and J.Z. are supported by the Penn State MRSEC for Nanoscale Science (DMR-2011839). Y.-F.Z., Z.Y. and C.-Z.C. are supported by the NSF-CAREER award (DMR-1847811) and Gordon and Betty Moore Foundation's EPiQS Initiative (GBMF9063 to C. Z. C.). C.D. and J.A.R. are supported by the Penn State NSF-MIP Two-Dimensional Crystal Consortium award (DMR-1539916). A.V. and J.A.R are supported by NSF-DMR 2002651. O.L. and Y.O. are supported by the BSF and NSF (2018643), the European Union's Horizon 2020 research and innovation programme (Grant Agreement LEGOTOP No. 788715), the DFG (CRC/Transregio 183, EI 519/7-1), and ISF Quantum Science and Technology (2074/19). K.W. and T.T. acknowledge support from JSPS KAKENHI (Grant Numbers 19H05790, 20H00354 and 21H05233). We thank Chao-Xing Liu, Ruobing Mei, Ying Liu for helpful discussions.

Author contributions:

C.L. and J.Z. designed the experiment. C.L. fabricated the devices and made the transport measurements under the supervision of J.Z.; Y.-F.Z., H.Y. and Z.Y. performed the MBE growth and ARPES measurements under the supervision of C.-Z.C.; A.V., S.K., C.D. and T.B. performed the CHet growth and SEM under the supervision of J.A.R; O.L. performed BTK modeling under the supervision of Y.O.; K.W. and T.T. synthesized the h-BN crystals; K.W. and H.W. performed FIB and TEM measurements; C.L. and J.Z. analyzed data; C.L. and J.Z. wrote the manuscript with input from all authors.

Competing financial interests:

The authors declare no competing financial interests.

References

1. Fu, L., Kane, C.L., Superconducting proximity effect and Majorana fermions at the surface of a topological insulator. *Phys. Rev. Lett.* **100**, 096407 (2008).
2. Alicea, J., New directions in the pursuit of Majorana fermions in solid state systems. *Rep. Prog. Phys.* **75**, 076501 (2012).
3. Kitaev, A.Y., Fault-tolerant quantum computation by anyons. *Ann. Phys. (N.Y.)* **303**, 2-30 (2003).
4. Beenakker, C.W.J., Search for Majorana Fermions in Superconductors. *Annu. Rev. Condens. Matter Phys.* **4**, 113-136 (2013).
5. Shabani, J., Kjaergaard, M., Suominen, H.J., Kim, Y., Nichele, F., Pakrouski, K., Stankevic, T., Lutchyn, R.M., Krogstrup, P., Feidenhans'l, R., Kraemer, S., Nayak, C., Troyer, M., Marcus, C.M., Palmstrom, C.J., Two-dimensional epitaxial superconductor-semiconductor heterostructures: A platform for topological superconducting networks. *Phys. Rev. B* **93**, 155402 (2016).
6. Gazibegovic, S., Car, D., Zhang, H., Balk, S.C., Logan, J.A., de Moor, M.W.A., Cassidy, M.C., Schmits, R., Xu, D., Wang, G.Z., Krogstrup, P., Veld, R.L.M.O.H., Zuo, K., Vos, Y., Shen, J., Bouman, D., Hojatei, B.S., Pennachio, D., Lee, J.S., van Veldhoven, P.J., Koelling, S., Verheijen, M.A., Kouwenhoven, L.P., Palmstrom, C.J., Bakkers, E.P.A.M., Epitaxy of advanced nanowire quantum devices. *Nature* **548**, 434–438 (2017).
7. Frolov, S.M., Manfra, M.J., Sau, J.D., Topological superconductivity in hybrid devices. *Nat. Phys.* **16**, 718-724 (2020).
8. Lutchyn, R.M., Sau, J.D., Das Sarma, S., Majorana Fermions and a Topological Phase Transition in Semiconductor-Superconductor Heterostructures. *Phys. Rev. Lett.* **105**, 077001 (2010).
9. Oreg, Y., Refael, G., von Oppen, F., Helical Liquids and Majorana Bound States in Quantum Wires. *Phys. Rev. Lett.* **105**, 177002 (2010).
10. Mourik, V., Zuo, K., Frolov, S.M., Plissard, S.R., Bakkers, E.P.A.M., Kouwenhoven, L.P., Signatures of Majorana Fermions in Hybrid Superconductor-Semiconductor Nanowire Devices. *Science* **336**, 1003-1007 (2012).

11. Wang, M.X., Liu, C.H., Xu, J.P., Yang, F., Miao, L., Yao, M.Y., Gao, C.L., Shen, C.Y., Ma, X.C., Chen, X., Xu, Z.A., Liu, Y., Zhang, S.C., Qian, D., Jia, J.F., Xue, Q.K., The Coexistence of Superconductivity and Topological Order in the Bi₂Se₃ Thin Films. *Science* **336**, 52-55 (2012).
12. Xu, J.P., Liu, C.H., Wang, M.X., Ge, J.F., Liu, Z.L., Yang, X.J., Chen, Y., Liu, Y., Xu, Z.A., Gao, C.L., Qian, D., Zhang, F.C., Jia, J.F., Artificial Topological Superconductor by the Proximity Effect. *Phys. Rev. Lett.* **112**, 217001 (2014).
13. Xu, J.P., Wang, M.X., Liu, Z.L., Ge, J.F., Yang, X.J., Liu, C.H., Xu, Z.A., Guan, D.D., Gao, C.L., Qian, D., Liu, Y., Wang, Q.H., Zhang, F.C., Xue, Q.K., Jia, J.F., Experimental Detection of a Majorana Mode in the core of a Magnetic Vortex inside a Topological Insulator-Superconductor Bi₂Te₃/NbSe₂ Heterostructure. *Phys. Rev. Lett.* **114**, 017001 (2015).
14. Sun, H.H., Zhang, K.W., Hu, L.H., Li, C., Wang, G.Y., Ma, H.Y., Xu, Z.A., Gao, C.L., Guan, D.D., Li, Y.Y., Liu, C.H., Qian, D., Zhou, Y., Fu, L., Li, S.C., Zhang, F.C., Jia, J.F., Majorana Zero Mode Detected with Spin Selective Andreev Reflection in the Vortex of a Topological Superconductor. *Phys. Rev. Lett.* **116**, 257003 (2016).
15. Zang, Y.Y., Kuster, F., Zhang, J.B., Liu, D.F., Pal, B., Deniz, H., Sessi, P., Gilbert, M.J., Parkin, S.S.P., Competing Energy Scales in Topological Superconducting Heterostructures. *Nano Lett.* **21**, 2758-2765 (2021).
16. Xu, S.Y., Alidoust, N., Belopolski, I., Richardella, A., Liu, C., Neupane, M., Bian, G., Huang, S.H., Sankar, R., Fang, C., Dellabetta, B., Dai, W.Q., Li, Q., Gilbert, M.J., Chou, F.C., Samarth, N., Hasan, M.Z., Momentum-space imaging of Cooper pairing in a half-Dirac-gas topological superconductor. *Nat. Phys.* **10**, 943-950 (2014).
17. Zhang, H., Ma, X.D., Li, L., Langenberg, D., Zeng, C.G., Miao, G.X., Two-step growth of high-quality Nb/(Bi_{0.5}Sb_{0.5})₂Te₃/Nb heterostructures for topological Josephson junctions. *J. Mater. Res.* **33**, 2423-2433 (2018).
18. Kurter, C., Finck, A.D.K., Hor, Y.S., Van Harlingen, D.J., Evidence for an anomalous current-phase relation in topological insulator Josephson junctions. *Nat. Commun.* **6**, 7130 (2015).
19. Flototto, D., Ota, Y., Bai, Y., Zhang, C., Okazaki, K., Tsuzuki, A., Hashimoto, T., Eckstein, J.N., Shin, S., Chiang, T.C., Superconducting pairing of topological surface states in bismuth selenide films on niobium. *Sci. Adv.* **4**, eaar721 (2018).
20. Williams, J.R., Bestwick, A.J., Gallagher, P., Hong, S.S., Cui, Y., Bleich, A.S., Analytis, J.G., Fisher, I.R., Goldhaber-Gordon, D., Unconventional Josephson Effect in Hybrid Superconductor-Topological Insulator Devices. *Phys. Rev. Lett.* **109**, 056803 (2012).

21. Kayyalha, M., Kargarian, M., Kazakov, A., Miotkowski, I., Galitski, V.M., Yakovenko, V.M., Rokhinson, L.P., Chen, Y.P., Anomalous Low-Temperature Enhancement of Supercurrent in Topological-Insulator Nanoribbon Josephson Junctions: Evidence for Low-Energy Andreev Bound States. *Phys. Rev. Lett.* **122**, 047003 (2019).
22. Dai, W.Q., Richardella, A., Du, R.Z., Zhao, W.W., Liu, X., Liu, C.X., Huang, S.H., Sankar, R., Chou, F.C., Samarth, N., Li, Q., Proximity-effect-induced Superconducting Gap in Topological Surface States - A Point Contact Spectroscopy Study of NbSe₂/Bi₂Se₃ Superconductor-Topological Insulator Heterostructures. *Sci. Rep.* **7**, 7631 (2017).
23. Briggs, N., Bersch, B., Wang, Y.X., Jiang, J., Koch, R.J., Nayir, N., Wang, K., Kolmer, M., Ko, W., Duran, A.D., Subramanian, S., Dong, C.Y., Shallenberger, J., Fu, M.M., Zou, Q., Chuang, Y.W., Gai, Z., Li, A.P., Bostwick, A., Jozwiak, C., Chang, C.Z., Rotenberg, E., Zhu, J., van Duin, A.C.T., Crespi, V., Robinson, J.A., Atomically thin half-van der Waals metals enabled by confinement heteroepitaxy. *Nat. Mater.* **19**, 637–643 (2020).
24. Zhang, J., Chang, C.-Z., Zhang, Z., Wen, J., Feng, X., Li, K., Liu, M., He, K., Wang, L., Chen, X., Xue, Q.-K., Ma, X., Wang, Y., Band structure engineering in (Bi_{1-x}Sb_x)₂Te₃ ternary topological insulators. *Nat. Commun.* **2**, 574 (2011).
25. Song, C.L., Wang, Y.L., Jiang, Y.P., Zhang, Y., Chang, C.Z., Wang, L.L., He, K., Chen, X., Jia, J.F., Wang, Y.Y., Fang, Z., Dai, X., Xie, X.C., Qi, X.L., Zhang, S.C., Xue, Q.K., Ma, X.C., Topological insulator Bi₂Se₃ thin films grown on double-layer graphene by molecular beam epitaxy. *Appl. Phys. Lett.* **97**, 143118 (2010).
26. Chang, C.Z., Tang, P.Z., Feng, X., Li, K., Ma, X.C., Duan, W.H., He, K., Xue, Q.K., Band Engineering of Dirac Surface States in Topological-Insulator-Based van der Waals Heterostructures. *Phys. Rev. Lett.* **115**, 136801 (2015).
27. Li, J., Leng, H.B., Fu, H.L., Watanabe, K., Taniguchi, T., Liu, X., Liu, C.X., Zhu, J., Superconducting proximity effect in a transparent van der Waals superconductor-metal junction. *Phys. Rev. B* **101**, 195405 (2020).
28. Li, H.Y., Ying, Z., Lyu, B.S., Deng, A.L., Wang, L.L., Taniguchi, T., Watanabe, K., Shi, Z.W., Electrode-Free Anodic Oxidation Nanolithography of Low-Dimensional Materials. *Nano Lett.* **18**, 8011-8015 (2018).
29. Bretheau, L., Joel, I., Wang, J., Pisoni, R., Watanabe, K., Taniguchi, T., Jarillo-Herrero, P., Tunnelling spectroscopy of Andreev states in graphene. *Nat. Phys.* **13**, 756-760 (2017).
30. Cascales, J.P., Martinez, I., Katmis, F., Chang, C.Z., Guerrero, R., Moodera, J.S., Aliev, F.G., Band structure of topological insulators from noise measurements in tunnel junctions. *Appl. Phys. Lett.* **107**, 252402 (2015).
31. Knispel, T., Jolie, W., Borgwardt, N., Lux, J., Wang, Z.W., Ando, Y., Rosch, A., Michely, T., Gruninger, M., Charge puddles in the bulk and on the surface of the topological

- insulator BiSbTeSe₂ studied by scanning tunneling microscopy and optical spectroscopy. *Phys. Rev. B* **96**, 195135 (2017).
32. Cyrot, M., Ginzburg-Landau theory for superconductors. *Rep. Prog. Phys.* **36**, 103 (1973).
 33. Talantsev, E.F., Crump, W.P., Tallon, J.L., Universal scaling of the self-field critical current in superconductors: from sub-nanometre to millimetre size. *Sci. Rep.* **7**, 10010 (2017).
 34. Blonder, G.E., Tinkham, M., Klapwijk, T.M., Transition from metallic to tunneling regimes in superconducting microconstrictions: Excess current, charge imbalance, and supercurrent conversion. *Phys. Rev. B* **25**, 4515-4532 (1982).
 35. Daghero, D., Gonnelli, R.S., Probing multiband superconductivity by point-contact spectroscopy. *Supercond. Sci. Technol.* **23**, 043001 (2010).
 36. Park, E., Lee, S., Ronning, F., Thompson, J.D., Zhang, Q., Balicas, L., Lu, X., Park, T., Spectroscopic evidence for two-gap superconductivity in the quasi-1D chalcogenide Nb₂Pd_{0.81}S₅. *J. Phys.: Condens. Matter* **30**, 165401 (2018).
 37. Suderow, H., Guillamon, I., Rodrigo, J.G., Vieira, S., Imaging superconducting vortex cores and lattices with a scanning tunneling microscope. *Supercond. Sci. Technol.* **27**, 063001 (2014).

Supplementary Information:

Proximity-Induced Superconductivity in Scalable Topological Insulator/Graphene/Gallium Heterostructures

Cequn Li¹, Yi-Fan Zhao¹, Alexander Vera^{2,3,4}, Omri Lesser⁵, Hemian Yi¹, Shalini Kumari^{2,3,4}, Zijie Yan¹, Chengye Dong^{2,3,4}, Timothy Bowen^{2,3,4}, Ke Wang⁶, Haiying Wang⁶, Kenji Watanabe⁷, Takashi Taniguchi⁸, Yuval Oreg⁵, Joshua A. Robinson^{2,3,6,9,10}, Cui-Zu Chang¹, and Jun Zhu^{1,2*}

1. Department of Physics, The Pennsylvania State University, University Park, PA 16802, USA
2. Center for 2-Dimensional and Layered Materials, The Pennsylvania State University, University Park, PA 16802, USA
3. Department of Materials Science and Engineering, The Pennsylvania State University, University Park, PA 16802, USA
4. Center for Nanoscale Science, The Pennsylvania State University, University Park, PA 16802, USA
5. Department of Condensed Matter Physics, Weizmann Institute of Science, Rehovot 760001, Israel
6. Materials Research Institute, The Pennsylvania State University, University Park, PA 16802, USA
7. Research Center for Functional Materials, National Institute for Materials Science, 1-1 Namiki, Tsukuba 305-0044, Japan
8. International Center for Materials Nanoarchitectonics, National Institute for Materials Science, 1-1 Namiki, Tsukuba 305-0044, Japan.
9. Department of Chemistry, The Pennsylvania State University, University Park, PA 16802, USA
10. 2-Dimensional Crystal Consortium, The Pennsylvania State University, University Park, PA 16802, USA.

* Correspondence to: jzhu@phys.psu.edu (J. Zhu)

Contents

1. Additional ARPES measurements	2
2. Fabrication of van der Waals tunnel junction	3
3. Four-terminal transport on BST/Gr/Ga.....	4
4. Fitting the tunneling spectra on Gr/Ga using the Blonder-Tinkham-Klapwijk model	6
5. Two-gap BTK fits on the 5QL and 10QL BST/Gr/Ga heterostructures.....	7
6. Vortex motion probed by tunneling conductance	11

1. Additional ARPES measurements

Figure S1 shows the ARPES band maps of 5-10QL $(\text{Bi}_{0.7}\text{Sb}_{0.3})_2\text{Te}_3/\text{Gr}/\text{Ga}$ (BST/Gr/Ga) heterostructures. In each panel, the Fermi level resides in the Dirac surface states of the $(\text{Bi}_{0.7}\text{Sb}_{0.3})_2\text{Te}_3$ film. The Dirac point shifts from -200 meV to -170 meV as the film thickness increases from 5QL to 10QL.

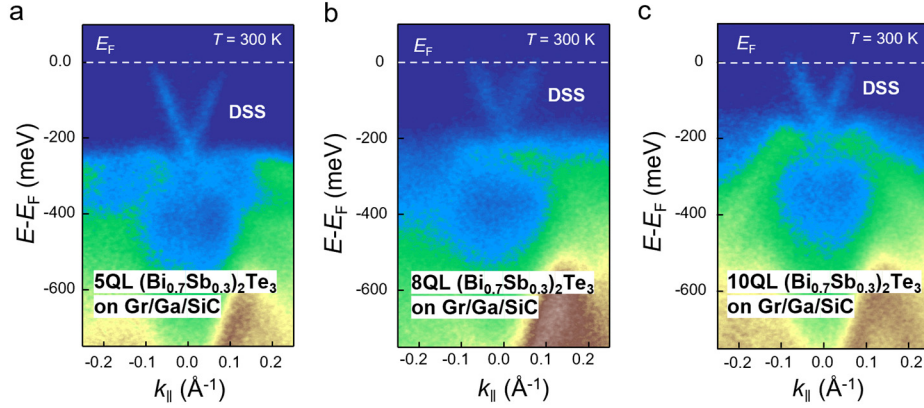


Fig. S1 | Room-temperature ARPES band maps of 5-10QL $(\text{Bi}_{0.7}\text{Sb}_{0.3})_2\text{Te}_3$ grown on Gr/Ga.

2. Fabrication of van der Waals tunnel junction

Figure S2 illustrates the steps we took to fabricate van der Waals (vdW) tunnel junctions on BST/Gr/Ga films. Grown films are transferred from the MBE chamber to an argon-filled glovebox using a vacuum suitcase with a base pressure of $\sim 5 \times 10^{-8}$ mbar and kept in the glovebox to avoid oxidization and contamination of the BST surface. We first etch a long graphite stripe (3-6 nm in thickness) into squares of approximately $3 \mu\text{m}^2$ in area using an atomic force microscope-based etching process¹ that avoids the use of polymer resists. These graphite squares serve as the top electrodes of the tunnel junction. We then construct an h-BN/graphite electrode/1-2L h-BN stack using vdW dry transfer techniques, a picture of which is shown in Fig. S2a. The stack is transferred to a BST/Gr/Ga film inside the glovebox. Next, we use standard lithographic techniques to deposit a 55-nm-thick Al_2O_3 film to surround the h-BN encapsulated area as shown in Fig. S2b. The Al_2O_3 film further protects the BST film from oxidization and also serves to isolate individual electrodes. We subsequently use e-beam lithography and established reactive ion etch recipe (CHF_3 40 sccm/ O_2 4 sccm) to open circular windows with radius about 250 nm on the top h-BN sheet to expose the graphite electrodes (Fig. S2c). Finally, we pattern and deposit 5-nm Ti/60-nm Au metal

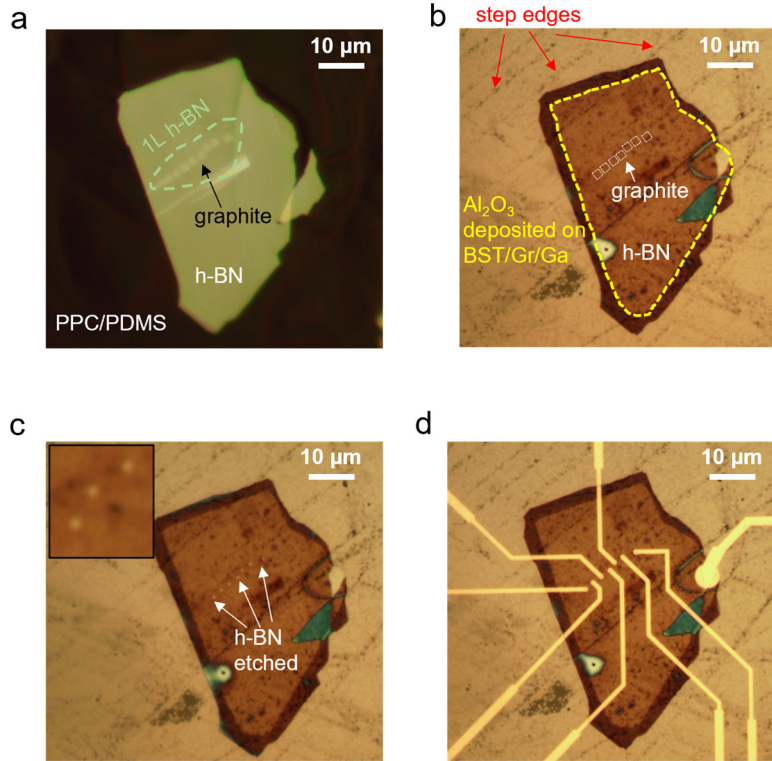


Fig. S2 | Fabrication of van der Waals tunnel junction on BST/Gr/Ga. **a**, A vdW stack of h-BN/graphite electrode/1L h-BN on a PPC/PDMS stamp. **b**, The stack transferred to the BST/Gr/Ga film and after the Al_2O_3 deposition. Outside the yellow dashed line, the BST/Gr/Ga film is covered with a 55nm-thick Al_2O_3 film. Red arrows point to step edges of the SiC substrate, where the intercalation of Ga may not be continuous. Tunnel junctions are placed within a single terrace. **c**, Circular windows of radius ~ 250 nm are etched into the top h-BN sheet to expose the graphite electrodes underneath. The inset shows a magnified image of a few windows. **d**, A completed device.

leads to connect to the graphite electrodes and the TI/Gr/Ga surface. A complete device is shown in Fig. S2d.

3. Four-terminal transport on BST/Gr/Ga

Four-terminal transport studies of BST/Gr/Ga films show that the growth of BST preserves very well the superconducting Ga layer underneath. Fig. S3a-c show the temperature and magnetic field-dependent resistance in films of varying BST film thickness and Table S1 summarizes their growth parameters and superconducting characteristics. Overall we find the superconducting transition temperature T_c of Ga varies between 3 to 4.2 K and the out-of-plane upper critical field H_{c2} ranges 50–80 mT, consistent with previous findings of Briggs et al². These measurements serve as reference to tunneling spectroscopy performed on the same films. Figure S3d plots the V - I data of a 5QL TI/Gr/Ga film, where a critical current of 200 μ A is observed. Although the current flow is limited to between the current leads, we can estimate the order of magnitude of the critical current density J_c using the width of the quasi-hall bar $W = 4.7 \mu\text{m}$ and a thickness of $d = 0.35 \text{ nm}$ for the 2L Ga film. $J_c = 0.14 \text{ A}/\mu\text{m}^2$ in this device, which is comparable to that of an elemental superconductor such as Al and Nb³. Measurements on other films show a typical J_c of 0.01–0.1 $\text{A}/\mu\text{m}^2$.

Film number	BST film thickness (QL)	x in $(\text{Bi}_x\text{Sb}_{1-x})_2\text{Te}_3$	T_c (K)	Out-of-plane H_{c2} (mT)
01	Gr/Ga	-	3.1	79
02	5	0.7	4	80
03	10	0.7	4.1	70
04	5	0.4	3.9	47
05	8	0.7	4.2	62
06	10	0.7	3.5	73

Table S1 | Thickness, stoichiometry and superconductivity parameters of BST/Gr/Ga films studied in this work. We defined the critical temperature T_c and the upper critical field H_{c2} as the temperature and magnetic field at which the sample reaches 90% of its normal state resistance, respectively.

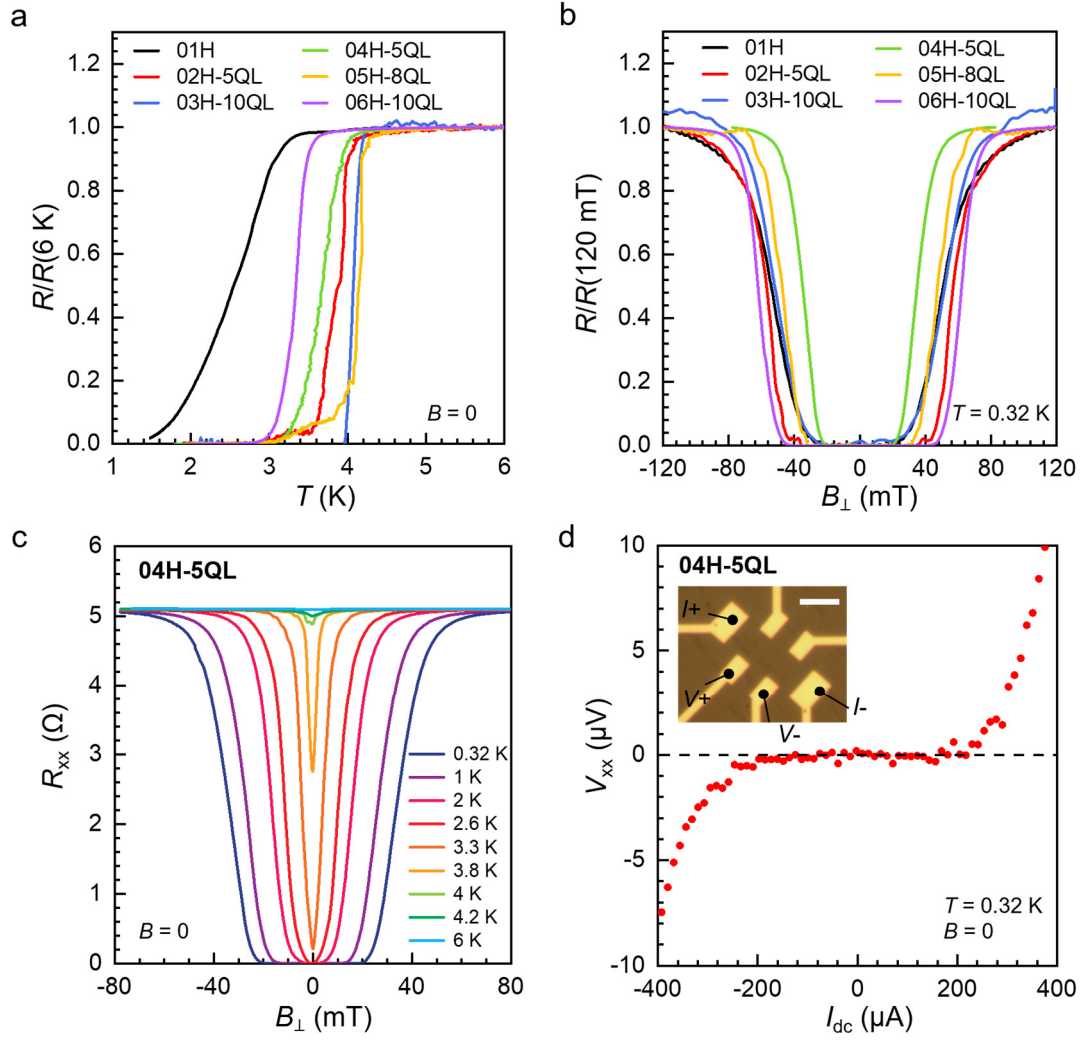


Fig. S3 | Transport studies of BST/Gr/Ga heterostructures. **a**, Normalized temperature-dependent resistance $R(T)$ in devices as labeled. 01-06 correspond to the film number in Table S1. **b**, Normalized magnetic field-dependent resistance $R(B)$ of the same devices in **a**. **c**, $R(B)$ on device 04H-5QL at selected temperatures. **d**, V_{xx} versus I_{dc} on device 04H-5QL showing a large critical current of $\sim 200\text{ }\mu\text{A}$. The inset shows an optical image of the device. Metal electrodes are directly evaporated on the BST/Gr/Ga film to form a quasi-Hall bar structure. Scale bar: $5\text{ }\mu\text{m}$.

4. Fitting the tunneling spectra on Gr/Ga using the Blonder-Tinkham-Klapwijk model

We fit the differential conductance dI/dV vs T to the Blonder-Tinkham-Klapwijk (BTK) model (Eqs. 1-3)⁴, which contains three important parameters, i.e. the superconducting gap Δ , the lifetime broadening Γ of the Cooper pairs and the tunnel barrier strength Z . A completely transparent barrier has $Z = 0$.

$$\frac{dI}{dV} = G_N \int_{-\infty}^{\infty} dE [1 + A(E) - B(E)] \frac{\partial f(E - eV)}{\partial(eV)} \Lambda(E), \quad (1)$$

where

$$A(E) = \begin{cases} \frac{\Delta^2}{(E + i\Gamma)^2 + (1 + 2Z^2)^2 [\Delta^2 - (E + i\Gamma)^2]}, & E < \Delta \\ \frac{u_0^2 v_0^2}{Y^2}, & E \geq \Delta \end{cases} \quad (2)$$

and

$$B(E) = \begin{cases} 1 - A(E), & E < \Delta \\ \frac{(u_0^2 - v_0^2)^2 Z^2 (1 + Z^2)}{Y^2}, & E \geq \Delta \end{cases} \quad (3)$$

with $u_0^2 = \frac{1}{2} \text{Re}(1 + \sqrt{\frac{(E+i\Gamma)^2 - \Delta^2}{(E+i\Gamma)^2}})$, $v_0^2 = \text{Re}(1 - u_0^2)$, and $Y^2 = [u_0^2 + Z^2(u_0^2 - v_0^2)]^2$. $f(E) = (1 + e^{E/k_B T})^{-1}$ is the Fermi-Dirac distribution function, and $\Lambda(E)$ is the empirical instrumental broadening term with the form of $\Lambda(E) = \sqrt{2\pi\sigma^2} \exp(-\frac{E^2}{2\sigma^2})$ where the variance σ is chosen to be 2.5 times the ac excitation $\sigma = 2.5V_{ac}$ following conventional practices. We have also produced fits with $\sigma = V_{ac}$ and $\sigma = 3V_{ac}$ and the changes to the fitting results are negligible. Eqs. 1-3 are implemented in MATLAB to fit data.

Figure S4 shows the full set of temperature- and magnetic field-dependent tunneling spectra acquired on device 01T (Fig. S4a-c), which is a Gr/Ga film without the BST growth, together with fits using the BTK model (Fig. S4d). The resulting T -dependent SC gap $\Delta(T)$, the tunnel barrier transparency Z and the lifetime broadening Γ of the Cooper pairs are given in Fig. S4e-f. $\Delta(T)$ is well described by the BCS theory, with a $T_c = 3.1$ K and $\Delta_0 = 0.395$ meV, consistent with four-terminal studies performed on the same film (See device 01H in Fig. S3). The tunnel barrier strength Z slightly decreases with increasing temperature while the lifetime broadening Γ increases somewhat with increasing T . These are consistent with naïve expectations. For instance, interaction with phonon modes at elevated temperatures may increase Γ while thermally assisted tunneling results in an apparent increase in the transparency of the tunnel barrier. Fitting parameters obtained here serve as reference and consistency check to analyses of the BST/Gr/Ga junctions.

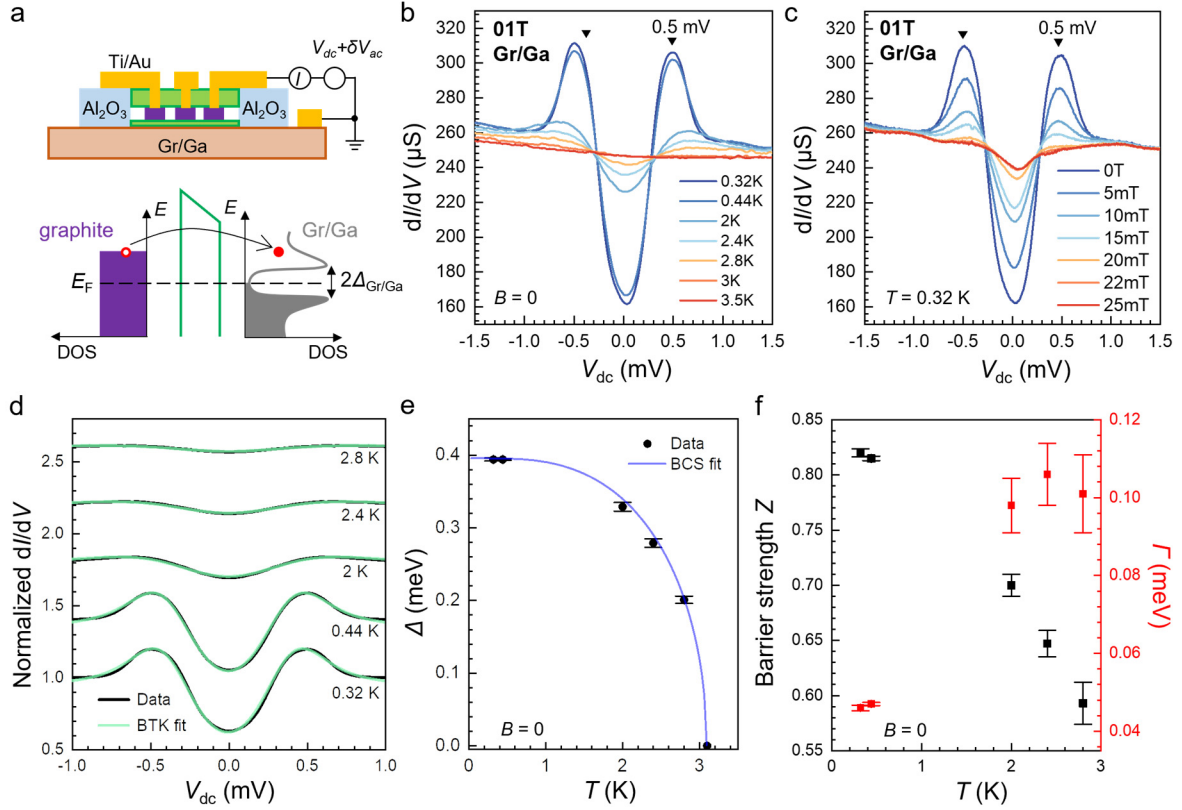


Fig. S4 | Fitting the superconducting tunneling spectra on Gr/Ga using the BTK model. **a**, Schematics of the tunneling junction and the tunneling process. **b**, **c**, dI/dV versus V_{dc} on device 01T at selected temperatures (**b**), and perpendicular magnetic fields (**c**). **d**, BTK fits at different temperatures. The fits capture data very well. **e**, $\Delta(T)$ obtained from fits in **d**. The blue solid line plots the BCS description of $\Delta(T) = \Delta_0 \tanh\left(1.74 \sqrt{\frac{T_c}{T}} - 1\right)$, where $T_c = 3.1$ K and $\Delta_0 = 0.395$ meV. **f**, The tunnel barrier strength parameter Z and lifetime broadening parameter Γ as a function of temperature obtained from the fits. Error bars represent 95% confidence interval of the fits.

5. Two-gap BTK fits on the 5QL and 10QL BST/Gr/Ga heterostructures

A two-gap BTK model^{5, 6} is used to fit the tunneling spectra in 5 and 10 QL TI/Gr/Ga heterostructures, where characteristics of two superconducting gaps are observed (Figs. S5 and S6). We consider the total tunneling current to be the sum of two contributions that originate from tunneling into the BST surface $(dI/dV)_S$ and the BST/Gr/Ga interface $(dI/dV)_I$ respectively:

$$(dI/dV)_{\text{total}} = f_S \times (dI/dV)_S + f_I \times (dI/dV)_I,$$

(4)

where $f_{S,I}$ represents the spectra weight of each contribution and $f_S + f_I = 1$. The two-gap fit contains 5 parameters, i.e., f_S , Δ_S , Δ_I , Γ_S , Γ_I and a common Z as it is mostly determined by the h-BN tunnel barrier.

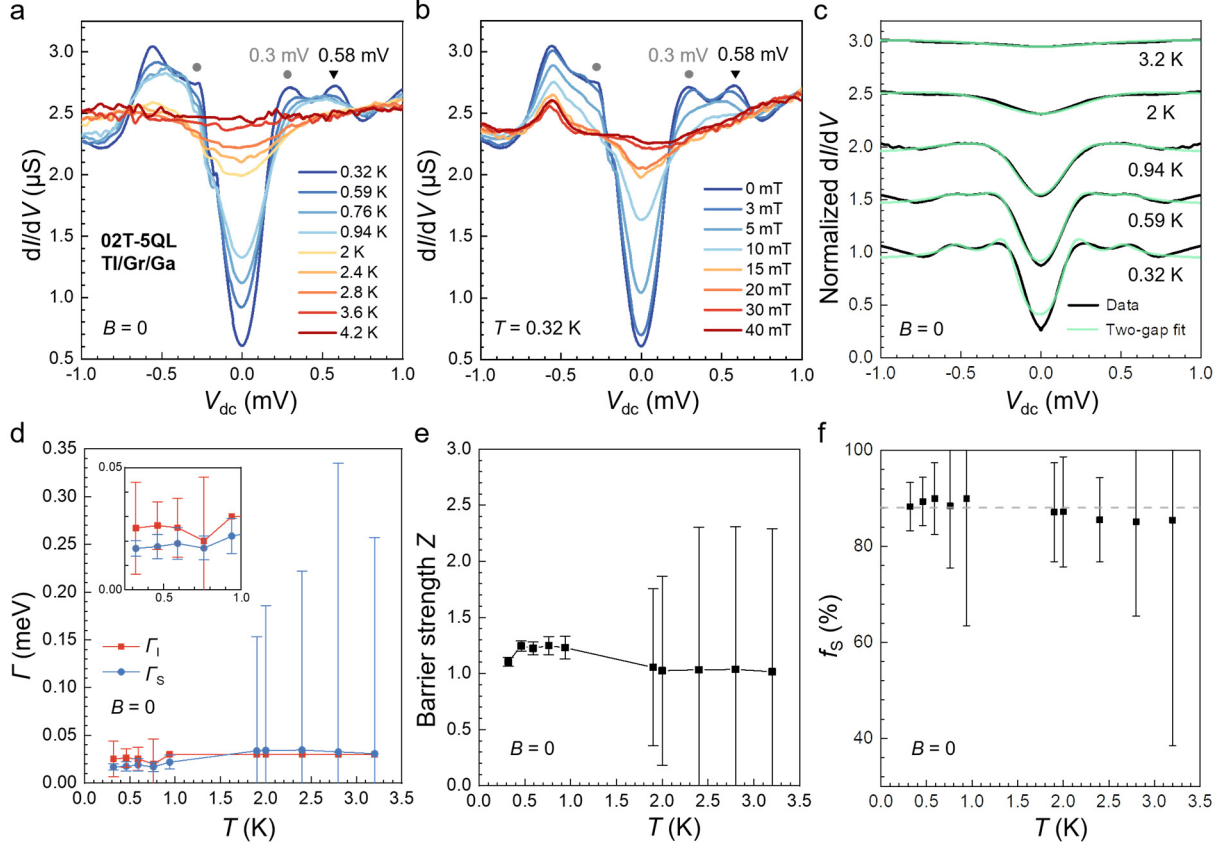


Fig. S5 | Tunneling spectra on device 02T-5QL and two-gap BTK fits. **a, b**, dI/dV versus V_{dc} at selected temperatures (**a**) and perpendicular magnetic field (**b**). **c**, Two-gap BTK fits to the data in **a** at selected temperatures. As the B -dependent spectra in **b** show, certain features on the negative bias side may not be related to superconductivity. We have therefore chosen to only fit data on the positive bias side in **c**. **d**, Lifetime broadening parameters Γ_S and Γ_I as a function of temperature. The low temperature value of $\Gamma_I \sim 0.03$ meV agrees with the results in Fig. S4 very well. To reduce fitting uncertainty, we have fixed $\Gamma_I \sim 0.03$ meV for $T \sim 1$ K and above, where $k_B T \gg \Gamma$ and thermal broadening dominates. This allows us to obtain fits for Γ_S , which comes out to be similar to Γ_I although with large uncertainties. Part of this uncertainty originates from the anti-correlation between Γ_S and the barrier strength Z . A large Z reduces the zero-bias conductance, which requires a smaller Γ_S to compensate. **e**, The barrier strength Z as a function of temperature. **f**, f_S as a function of temperature showing that on average, tunneling into the TI surface contributes 88% of the spectra weight. Error bars represent 95% confidence interval of the fits.

Fig. S5 show the T -dependent and B -dependent tunneling spectra taken on device 02T-5QL, the BTK fits, and the parameters obtained from the fits. The main results, i.e. $\Delta_S(T)$ and $\Delta_I(T)$, are shown in Fig. 3 of the main text. Figs. S5d-f plot the remaining fitting parameters. The two-gap fits yield robust values of Δ_S and Δ_I , especially at low temperatures, as their values are dictated by prominent features of the data such as the V shape near zero bias and the appearance of a second

coherence peak. A barrier strength of $Z \sim 1$ is consistent among all the junctions we analyzed (Figs S4-6). The results for the lifetime broadening parameters are less reliable at $T > 1$ K where features become broadened and independent determinations become difficult. Nonetheless, they are consistent with results obtained on Gr/Ga junctions (Fig. S4) and on a 10QL BST/Gr/Ga heterostructure (Fig. S6). Our fits show that the measured dI/dV is dominated by the tunneling into the TI surface states, with $f_S \sim 0.9$. This is also reasonable, given that an electron reaching the Gr/Ga interface needs to traverse the semi-insulating $(\text{Bi}_{0.7}\text{Sb}_{0.3})_2\text{Te}_3$ bulk.

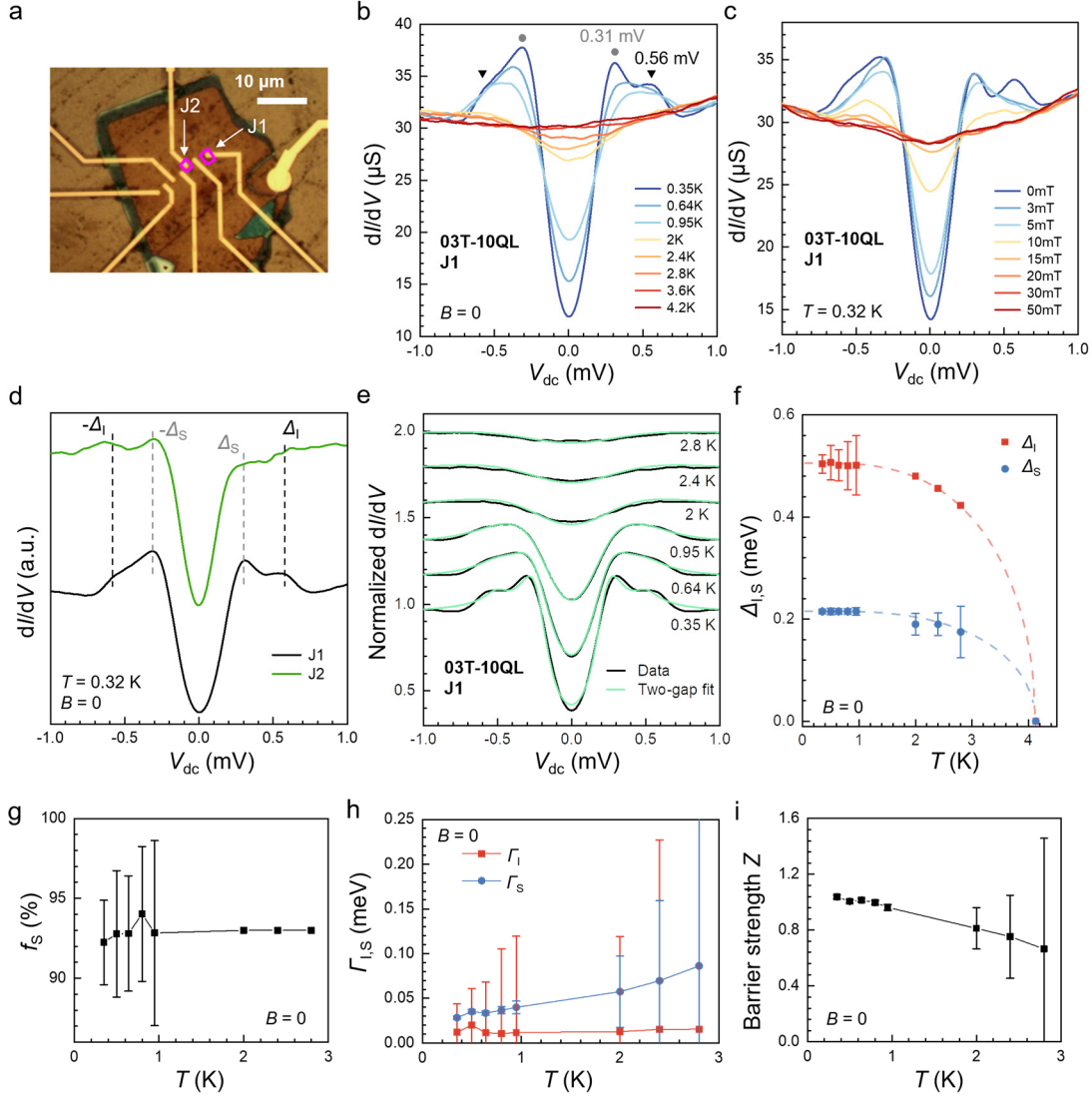


Fig. S6 | Tunneling spectra on device 03T-10QL and two-gap BTK fits. **a**, Optical image of 03T-10QL made on a 10QL ($\text{Bi}_{0.7}\text{Sb}_{0.3}$)/Gr/Ga film. J1 and J2 are two independent junctions. **b**, **c**, dI/dV versus V_{dc} at selected temperatures (**b**) and perpendicular magnetic fields (**c**) from J1. **d** plots the $T = 0.32$ K dI/dV traces from both junctions J1 and J2. Curves are normalized by their normal state conductance and stacked vertically for clarity. **e**, Two-gap BTK fits to the data in **a** at selected temperatures. Only data at positive biases are analyzed. Data at negative biases are replica of the positive side. **f**, $\Delta_S(T)$ and $\Delta_I(T)$ obtained from the fits in **e**. The red and blue dashed lines represent fits to the temperature dependence of a BCS gap with a common $T_c = 4.1$ K, similar to Fig. 3e of the main text. **g**, f_S as a function of temperature showing that below 1 K, 93% of the tunneling current goes into the TI surface. Above 2 K, f_S is fixed at 0.93 to enable more accurate fits for other parameters. **h**, Lifetime broadening parameters Γ_S and Γ_I as a function of temperature. Values obtained here are consistent with those found in Figs. S4 and S5. **i**, Barrier strength Z as a function of temperature, which is also consistent with other junctions studied. Error bars represent 95% confidence interval of the fits.

Similar tunneling spectroscopy measurements and analysis are performed on two other T-5QL junctions made on film 02 and two T-10QL junctions made on film 03. Features associated with two SC gaps are consistently observed in all of our devices, confirming that a proximity-induced gap opening in the surface states of the BST film is a robust finding of our experiment. The measurements and analysis of 03T-10QL are shown in Fig. S6.

Table S2 summarizes the proximity-induced Δ_S and the primary superconducting gap Δ_I obtained in different tunnel junctions made on BST films of different thicknesses d . The thickness dependence of Δ_S is not evident, likely due to the local variations of the film thickness under each junction. A study of $\Delta_S(d)$ will require a more precise control of the film thickness.

BST film thickness (QL)	T_c (K)	Junction	Δ_I (meV)	Δ_S (meV)	Δ_S/Δ_I (%)
0	3.1	01T	0.395 ± 0.003	-	-
5	4	G ₁₅ of 02T-5QL	0.5 ± 0.03	0.19 ± 0.01	37 ± 4
		G ₂₅ of 02T-5QL	0.49 ± 0.05	0.2 ± 0.003	41 ± 4
		G ₄₅ of 02T-5QL	0.51 ± 0.03	0.23 ± 0.01	46 ± 5
10	4.1	J1 of 03T-10QL	0.5 ± 0.02	0.215 ± 0.004	42 ± 2
		J2 of 03T-10QL	0.5 ± 0.03	0.17 ± 0.01	34 ± 4

Table S2 | Δ_I , Δ_S , and the ratio Δ_S/Δ_I found in different devices. $\Delta_I = \Delta_0$ in Gr/Ga.

6. Vortex motion probed by tunneling conductance

Discrete zero-bias conductance changes and hysteresis in B -field sweep due to the bunching and trapping of Abrikosov vortices are commonly observed in Gr/Ga and BST/Gr/Ga films we studied. Fig. S7a, c provide additional examples in devices 01T Gr/Ga and 02T-5QL BST/Gr/Ga. We identify the unit of conductance change G_{sv} , which all other conductance jumps are multiple integers of, and attribute it to the entry/exit a single vortex. This enables us to calculate the number of vortices N_{vortex} in the tunnel junction using

$$N_{\text{vortex}} = \frac{G(B) - G(0T)}{G_{sv}}, \quad (5)$$

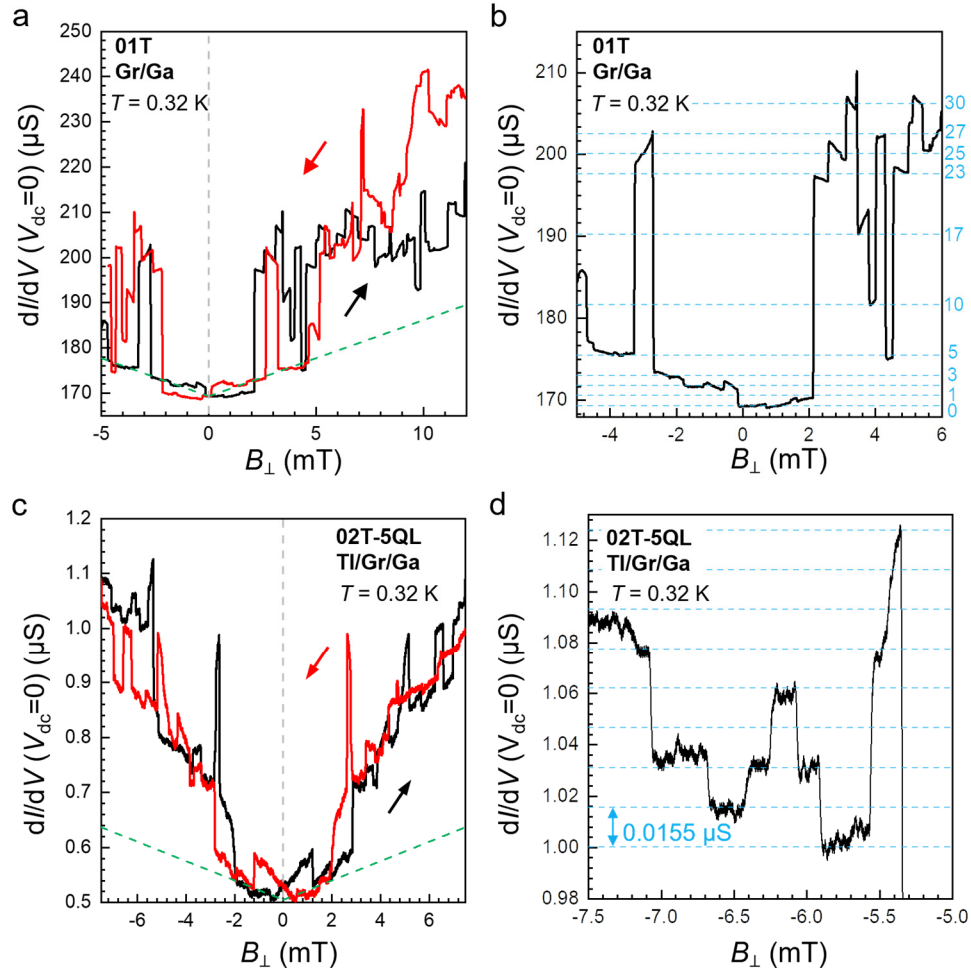


Fig. S7 | Single vortex motion and vortex pinning in Gr/Ga and TI/Gr/Ga films. **a**, Zero-bias dI/dV versus B_{\perp} in device 01 T (**a**) and 02T-5QL (**c**) showing hysteresis and discrete conductance jumps. The green dashed line is the calculated $\Delta G/\Delta B$ using Eq. (6) and the junction area $A = 2.82 \mu\text{m}^2$ in **a** and $A = 2.49 \mu\text{m}^2$ in **c**. The magnetic field is swept at a slow rate of 5–10 $\mu\text{T/s}$ to allow for the establishment of steady state. $T = 0.32$ K. **b**, Conductance plateaus in **a** are labeled by N_{vortex} given by Eq. (5). $G_{\text{sv}} = 1.23 \mu\text{S}$. **d**, Expanded data around $B_{\perp} = -6.5$ mT in **c** showing discrete conductance jumps in units of 1, 2, and 3 G_{sv} , where $G_{\text{sv}} = 0.0155 \mu\text{S}$ corresponds to the minimum conductance jump due to a single vortex.

We label N_{vortex} corresponding to individual conductance plateaus in device 01T in Fig. S7b. Fig. S7d shows examples of 1, 2, and 3 vortex-induced conductance change in 02T-5QL. As B increases, the number of vortices increases following $\Phi = B \times A = N_{\text{vortex}} \times \Phi_0$, where A is the tunnel junction area given by the top graphite electrode and $\Phi_0 = 2.068 \text{ mT} \cdot \mu\text{m}^2$ is the magnetic flux quantum. Together with Eq. (5), we obtain the average rate of conductance change vs B -field:

$$\frac{\Delta G}{\Delta B} = \frac{A \times G_{\text{sv}}}{\Phi_0}.$$

(6)

Eq. (6) is plotted as a green dashed line in Figs. S7a and c for devices 01T and 02T-5QL respectively. They capture the trend of data around $B = 0$ quite well. At B greater than a few mT, the conductance fluctuates both up and down with large amplitude, suggesting vortices move in and out of the tunnel junction area as bundles⁷. We expect that defects, such as domain walls in the film, to play an important role in the bunching and pinning of the vortices and details will vary from film to film and junction to junction. Indeed, Fig. S8 compares J1 and J2 made on the same film 03. J1 exhibits much larger conductance fluctuations than J2, suggesting stronger pinning effects.

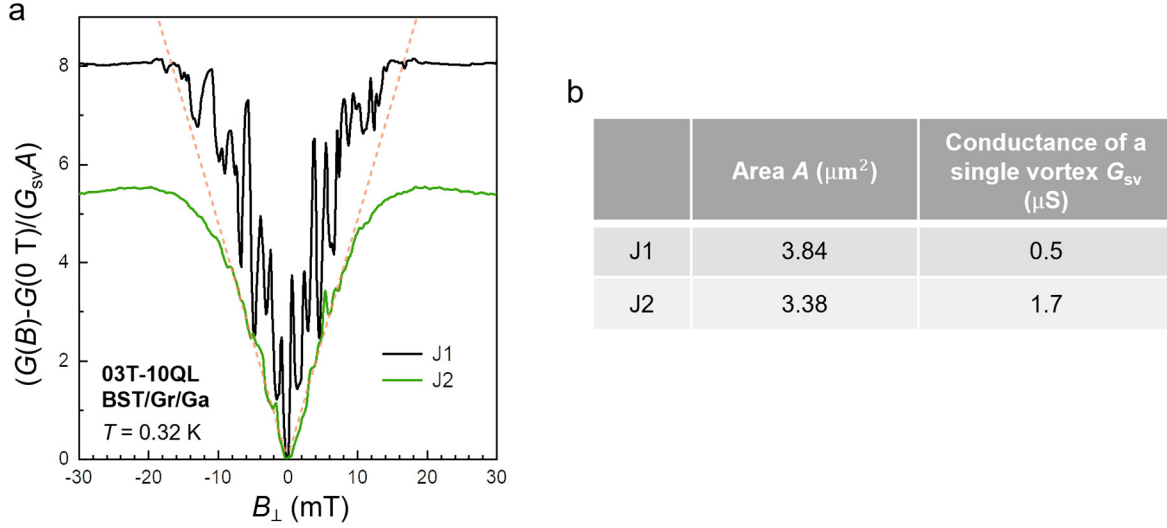


Fig. S8 | Vortex pinning in different junctions made on 03T-10QL. **a**, plots the vortex density N_{vortex}/A calculated from $\frac{G(B)-G(0\text{ T})}{G_{sv} \times A}$ for junctions J1 and J2, respectively. The orange dashed line plots B/Φ_0 . By definition, $N_{\text{vortex}}/A = B/\Phi_0$. J2 follows the orange dashed line very well, indicating smooth motion of the Abrikosov vortex lattice while J1 exhibits large deviations from the expected rate, suggesting strong pinning effects. Field sweep rate: 100 $\mu\text{T/s}$. Parameters used in the analysis are given in **b**. Data of J2 are shown in Fig. 4b of the main text.

References

- Li, H.Y., Ying, Z., Lyu, B.S., Deng, A.L., Wang, L.L., Taniguchi, T., Watanabe, K., Shi, Z.W., Electrode-Free Anodic Oxidation Nanolithography of Low-Dimensional Materials. *Nano Lett.* **18**, 8011-8015 (2018).
- Briggs, N., Bersch, B., Wang, Y.X., Jiang, J., Koch, R.J., Nayir, N., Wang, K., Kolmer, M., Ko, W., Duran, A.D., Subramanian, S., Dong, C.Y., Shallenberger, J., Fu, M.M., Zou, Q., Chuang, Y.W., Gai, Z., Li, A.P., Bostwick, A., Jozwiak, C., Chang, C.Z., Rotenberg,

- E., Zhu, J., van Duin, A.C.T., Crespi, V., Robinson, J.A., Atomically thin half-van der Waals metals enabled by confinement heteroepitaxy. *Nat. Mater.* **19**, 637–643 (2020).
3. Talantsev, E.F., Crump, W.P., Tallon, J.L., Universal scaling of the self-field critical current in superconductors: from sub-nanometre to millimetre size. *Sci. Rep.* **7**, 10010 (2017).
 4. Blonder, G.E., Tinkham, M., Klapwijk, T.M., Transition from metallic to tunneling regimes in superconducting microconstrictions: Excess current, charge imbalance, and supercurrent conversion. *Phys. Rev. B* **25**, 4515-4532 (1982).
 5. Daghero, D., Gonnelli, R.S., Probing multiband superconductivity by point-contact spectroscopy. *Supercond. Sci. Technol.* **23**, 043001 (2010).
 6. Park, E., Lee, S., Ronning, F., Thompson, J.D., Zhang, Q., Balicas, L., Lu, X., Park, T., Spectroscopic evidence for two-gap superconductivity in the quasi-1D chalcogenide Nb₂Pd_{0.81}S₅. *J. Phys.: Condens. Matter* **30**, 165401 (2018).
 7. Suderow, H., Guillamon, I., Rodrigo, J.G., Vieira, S., Imaging superconducting vortex cores and lattices with a scanning tunneling microscope. *Supercond. Sci. Technol.* **27**, 063001 (2014).